JOURNAL OF Materials CHEMISTRY

Magnetic Fe_2O_3–Al_2O_3 composites prepared by a modified wet impregnation method

Michael A. Karakassides,*[a] Dimitrios Gournis,[a] Athanasios B. Bourlinos,[a] Pantelis N. Trikalitis[b] and Thomas Bakas[c]

[a]*Department of Materials Science and Engineering, University of Ioannina, GR-45110, Ioannina, Greece. E-mail: mkarakas@cc.uoi.gr; Fax: +30 26510 97081; Tel: +30 26510 97276*
[b]*Department of Chemistry, Michigan State University, East Lansing, MI 48823, USA*
[c]*Physics Department, University of Ioannina, GR-45110, Ioannina, Greece*

Received 19th November 2002, Accepted 27th January 2003
First published as an Advance Article on the web 18th February 2003

Fe_2O_3–Al_2O_3 composites were prepared by interaction of acetic acid vapors with iron oxides dispersed on the surface of a sol–gel derived porous alumina. Upon pyrolysis the created iron acetate species were transformed to magnetic iron oxide nanoparticles. The atmosphere which is used during the synthetic procedure affects significantly the nature of the nanoparticles which could be either γ-Fe_2O_3 or magnetite, or non-magnetic such as α-Fe_2O_3. X-Ray diffraction, surface area measurements and scanning electron microscopy (SEM) were used for the structural characterization and determination of the sorption properties of the composite material properties. The development of magnetic phases decreases the specific surface area of alumina by seeding of the alumina particles and, in parallel, the coverage of their free surface. Mössbauer spectroscopy, magnetic measurements and transmission electron microscopy (TEM) provide evidence for the formation, size and type of magnetic iron oxide phases.

Introduction

It is well known that porous ceramics are used in a wide range of applications including catalysts, effective absorbents, ionic conductors, filtering membranes, coatings and insulating aerogels.[1–4] On the other hand, there is a great deal of interest in the preparation of nanosize magnetic particles and understanding of their properties, which are drastically different from those of the corresponding bulk materials.[5–7] These nanosize magnets are used in potential applications such as information storage, color imaging, magnetic refrigeration, ferrofluids *etc*.[8–11] Combining the above two kinds of materials it is possible to develop new ceramic–nanoceramic composites endowed with synergetic and improved properties. For example, in the environmental and biotechnology fields such composites could be used as absorbents and magnetic supports of high effectiveness because of their ability to be prepared in granular or other engineered forms.[12–15]

There are usually two chemical methods for the preparation of nanomagnetic ceramic composites: (a) *sol–gel synthesis*, where the magnetic phase is formed *in situ* inside a ceramic matrix, using precursors such as salts, complexes or alkoxides in the form of colloidal magnetic oxides. This route minimizes the aggregation of the magnetic oxide particles upon thermal treatment and thus imposes an upper limit on their size; (b) *wet impregnation of a salt solution on a ceramic support*: the impregnated support is then calcined to produce a composite material constituted of a ceramic matrix and an assembly of magnetic nanoparticles. Other methods have also been developed depending on the nature of the ceramic matrix and the magnetic oxides, involving some special apparatus,[16–18] sputtering[19,20] or using microemulsions.[21] Recently, a new method was used for developing magnetic clays[22] and silica–maghemite composites.[23] This method is based on route (b) in conjunction with the ability of iron carboxylate compounds to transform upon pyrolysis into crystalline magnetic phases.[24,25] More specifically, the carboxylate species were synthesized by wet impregnation of the appropriate amount of $Fe(NO_3)_3{\cdot}9H_2O$ salt solution on a porous matrix followed by exposure to vapors of acetic acid. Finally, calcination of the porous matrix and the carboxylate guest compound at 500 °C leads to the preparation of magnetic composites. We used the latter method in order to prepare Al_2O_3–Fe_2O_3 nanocomposites. These materials could be used in the development of new magnetically stabilized fluidized beds (MSFB) as bioreactors[26,27] for the chemical and biochemical industries. For example magnetizable biosupports with activated carbon and natural zeolites have been developed in the last few years[28] and have been tested as carriers for immobilized yeast cells for continuous ethanol production.[29] The new composites allow a decrease of the particle size toward that applied for conventional enzyme immobilization, combine high magnetic susceptibility with low permanent magnetization, a commercially available non-magnetic matrix and promise to avoid the negative effects of higher dissolution rates in the bioreactors.

Alumina is one of the widely used technical ceramics. We used the sol–gel technique to prepare the necessary alumina matrix since with this method it is possible to obtain Al_2O_3 in granular form having high specific surface area and very good thermal stability.[30] Due to these characteristics porous alumina is generally the first choice as a catalyst carrier. Although alumina is used very frequently as a ceramic matrix for metal–composite materials, only a few works have been published concerning its participation in magnetic composites. Along these lines maghemite formation on aluminium oxide has been obtained by dispersing iron(III) hydroxoacetate on the aluminium oxide and heating strongly.[31] Films from γ-alumina doped with γ-Fe_2O_3 particles were also prepared using poly(vinyl alcohol)–alumina hydrate precursors and sol–gel chemistry.[32] Fe_2O_3-containing aluminas were also prepared using a crystalline precursor derived from ammonium dawsonite.[33] Preparing such materials is of true value because γ-Fe_2O_3 (maghemite) is one of the most frequently used ferromagnetic materials for recording. It is known that

γ-Fe_2O_3 is an oxidation product of magnetite (Fe_3O_4), while the same compound in the form of fine particles has become a subject of considerable interest concerning both its preparation and its magnetic properties.

In the present work our efforts were focused on preparing a composite material consisting of magnetic iron oxide nanoparticles and porous alumina. The preparation stages and the structure of composites were examined using X-ray diffraction (XRD), surface area measurements and electron microscopy (SEM and TEM). The nature of the magnetic particles and their magnetic behavior were examined by means of Mössbauer spectroscopy and magnetic measurements over a wide temperature range.

Experimental

Materials

The porous alumina used as matrix for the preparation of magnetic composites was prepared by means of sol–gel chemistry following the method described by Vazquez.[34] The as-produced gel was dried in air under ambient conditions for 24 h and then heated at 450 °C. This product (porous alumina) was used as the porous matrix for the magnetic composite preparation due to its high surface area.

0.3 g of porous alumina was dispersed in 10 ml CH_3OH containing 606 mg of $Fe(NO_3)_3{\cdot}9H_2O$ (Merck) to produced samples containing 17% wt iron. The mixture was stirred for 1 h followed by rapid removal of the solvent at 80 °C. The as-prepared solid was powdered and exposed to vapors of acetic acid (99.5% Merck) at 80 °C for 1 h. The obtained sample was dried for 15 min at 80 °C in order to remove any physically absorbed acetic acid. Three different products were obtained by calcination for 1 h at 400 °C in air (Almag-air17), in nitrogen (Almag-N17) and in oxygen (Almag-O17) in order to examine the role of the calcination conditions in the magnetic and structural properties of the final products.

Techniques

X-Ray powder diffraction data were collected on a D8 ADVANCE BRUKER diffractometer using CuKα (40 kV, 40 mA) radiation and a secondary beam graphite monochromator. Diffraction patterns were collected in the 2Θ range from 10 to 90 degrees, in steps of 0.01 degrees and 1 s counting time per step. Scanning electron images were recorded using a JEOL JSM-6400V scanning electron microscope (SEM). The samples were gold sputtered to avoid charging effects on the images. Transmission electron micrographs were obtained with a JEOL 120CX instrument equipped with a CeB_6 filament and operating at 120 kV. TEM samples were prepared by gently grinding the powders and casting on a holey carbon grid. The images are typical and representative of the samples under observation.

Mössbauer spectra were recorded with a conventional constant acceleration spectrometer and a ^{57}Co(Rh) source and the parameters were obtained by a least-squares minimization program assuming Lorentzian line shapes. The Mössbauer spectrometer was calibrated with an α-Fe absorber and all isomer shift values reported here are relative to iron at room temperature.

Magnetic measurements were carried out at room temperature in a Quantum Design Magnetometer (SQUID), while the samples were measured in their powder form. Thermal variations of zero field cooled (ZFC) and field cooled (FC) magnetization curves were taken from 250 K to 4.2 K.

The N_2 adsorption–desorption isotherms were measured at 78 K on a Quantachrome Autosorb–I porosimeter. Specific surface areas S_{BET} were determined with the Brunauer–Emmett–Teller (BET) method using adsorption data points in the relative pressure P/P_o range 0.01 to 0.30. The desorption branches of the isotherms were used for the pore size calculations according to the Kelvin equation $r_k = 4.146/\log P_o/P$ (Å), where P_o is the saturated vapour pressure in equilibrium with the adsorbate condensed in a capillary or a pore, P is the vapour pressure of a liquid contained in a cylindrical capillary, and r_k is the Kelvin radius of the capillary or pore. All samples used for the surface analyses were outgassed at 250 °C for 10 h under high vacuum (10^{-5} mbar) before the measurements.

Results and discussion

Structural characterization and sorption properties

Fig. 1 presents the XRD patterns of Almag-air17, Almag-N17 and Almag-O17 samples along with porous alumina. The positions of the diffraction lines of γ-Fe_2O_3, magnetite (Fe_3O_4) and α-Fe_2O_3 are also indicated. As shown in this figure, the patterns of Almag-air17 and Almag-N17 exhibit a broad relatively intense reflection near 35.7°, clearly separated from the amorphous part, which can be attributed to the formation of nanophase γ-Fe_2O_3 or magnetite particles.[23] Using the Scherrer equation, the particle size of these particles can be estimated to be about 7–10 nm. On the other hand, the XRD pattern of Almag-O17 contains the characteristic reflections of α-Fe_2O_3 (stronger lines) and also of γ-Fe_2O_3 or magnetite (weaker lines). From the full width at half maximum (FWHM) of the sharp reflections in this pattern, using as above the Scherrer equation, the particle size of the α-Fe_2O_3 can be estimated to be about 40–60 nm. However, it is difficult to assign the observed reflections, in the above patterns, to γ-Fe_2O_3 or magnetite nanoparticles, since both phases show similar XRD patterns.

The surface area and the pore structure of our samples were determined from nitrogen isotherm analysis. As shown in Fig. 2 the porous alumina displayed a type-IV isotherm, charac- teristic for mesoporous materials, while hysteresis was observed indicating the occurrence of capillary condensation in the pores. Using these data, the specific surface area S_{BET} was calculated to be 514 $m^2\ g^{-1}$, the pore size 52 Å, and the total pore volume 0.59 mL g^{-1}. On the other hand, the magnetic composites, which were prepared using the above porous alumina as a ceramic matrix, displayed similar type-IV isotherms but the curves at high P/P_o values were flatter and

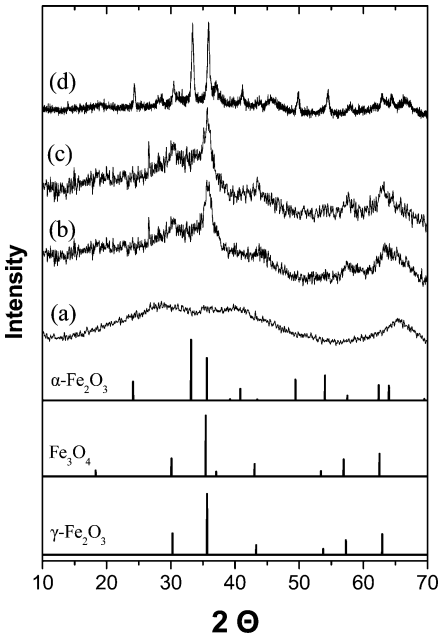

Fig. 1 XRD patterns of porous Al_2O_3 (a) and magnetic composites Almag-air17 (b), Almag-N17 (c), and Almag-O17 (d).

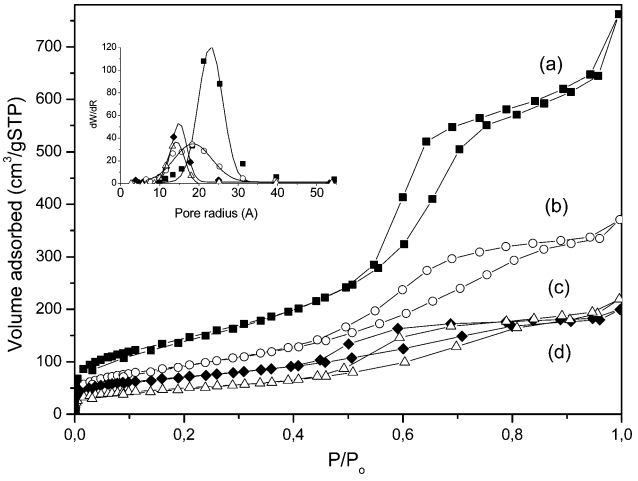

Fig. 2 Nitrogen adsorption–desorption isotherms of the samples: porous Al_2O_3 (a), Almag-air17 (b), Almag-N17 (c) and Almag-O17 (d). Inset, pore size distribution calculated from the N_2-desorption branch.

showed greater hysteresis. The total adsorbed N_2 volume was under 0.3 mL g^{-1} for the three composites (Fig. 2). Using these data, smaller effective pore radii and specific surface areas S_{BET} under 330 m^2 g^{-1} were obtained (Table 1). Among the three composites, the Almag-air17 sample appears to have the largest specific surface area. Although the reduction of S_{BET} for all magnetic composites is predictable, since the development of magnetic particles inside the porous alumina restricts the free surface of the solids, the reason for the observed differences in the sorption properties among them is not obvious. Probably the different atmospheric conditions during each composite preparation lead to a different morphology of each sample, which affects the sorption properties of the samples.

The particle morphology in the samples at the micrometer scale length was investigated using scanning electron microscopy (SEM). Shown in Fig. 3 are typical images of the as-synthesized host material (porous alumina) and the different composites. The images reveal a striking difference on the overall microstructure between the host material and the composites. In particular, porous alumina consists of irregularly shaped particles with sizes in the range of 1–70 μm, typical of highly porous alumina. In contrast, the nanocomposites show a more compact structure consisting of smaller particles (*ca.* <25 μm). Among the three nanocomposites, Almag-O17 shows the less porous structure. The microstructures of Almag-N17 and Almag-air17 samples have similar morphology and larger pores than Almag-O17. The difference between the host alumina matrix and composite materials originates from seeding effects of the iron oxide particles, which are used as precursors for the nanocomposite's preparation. In fact, it is well known that various oxides, including hematite, play the seeding role in nucleation and growth of α-Al_2O_3 from boehmite.[35,36] The initiation of transformation in porous alumina demands sufficient energy which must be supplied to the system in order to exceed the nucleation barrier. As the existence of iron oxide particles in the composites supplies the system with nuclei, the nucleation step effectively is eliminated, and as a result less energy is required for the transformation,

Table 1 Specific areas and pore sizes of alumina magnetic composites

Sample	S_{BET}/ m^2 g^{-1}	Pore diameter/Å	Total pore volume/mL g^{-1}
Alumina	514	52	0.59
Almag-N17	247	30	0.19
Almag-O17	173	28	0.12
Almag-air17	328	44	0.30

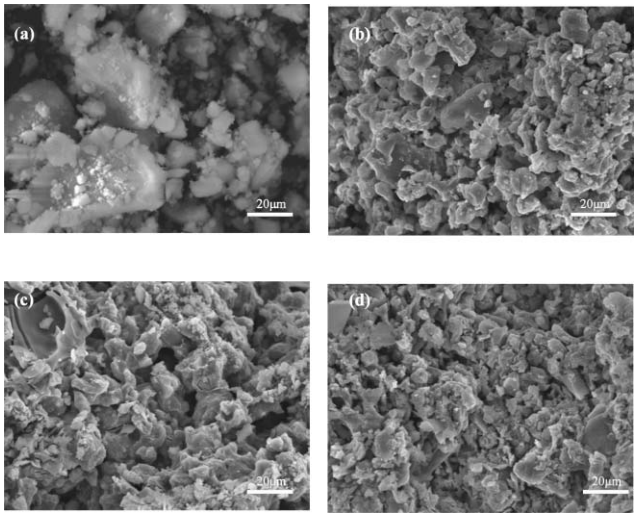

Fig. 3 Scanning electron micrographs of the samples: porous Al_2O_3 (a), Almag-air17 (b), Almag-N17 (c) and Almag-O17 (d).

which therefore occurs at a lower temperature. Probably the transformation of porous alumina to the γ-form starts at lower temperature resulting in different microstructures in the porous alumina and in the magnetic composites (Fig. 3).

Magnetic measurements and mechanism of formation of magnetic nanocomposites

Fig. 4 shows the magnetization curves *versus* the applied magnetic field at room temperature for the Almag composites. These curves are typical of samples possessing magnetic properties. By extrapolation, we deduce the following saturation magnetization values for the three composites: Almag-N17, $\sim$6.5 emu g^{-1}; Almag-air17, $\sim$3 emu g^{-1}; and Almag-O17, $\sim$2 emu g^{-1}. Taking into consideration that the nominal iron loading in the three composites is the same (17% wt), one can attribute the differences in the magnetization of the composites to other reasons. In fact it seems that the atmospheric conditions which were used during the composite preparation are very important. As reported earlier[25] the mechanism leading to the magnetic phase formation over the alumina support is based on the ability of the iron–carboxylate compounds to be transformed upon pyrolysis to crystalline magnetic iron oxidic nanoparticles. For instance, it is known that pyrolysis in air of the salt $Fe(NO_3)_3 \cdot 9H_2O$ at 300 °C leads to the formation of the non-magnetic α-Fe_2O_3 (hematite).[37–40] In contrast, the trinuclear iron complex $[Fe_3Ac_6O \cdot 3H_2O]NO_3$, prepared according to a published route,[41] affords pure

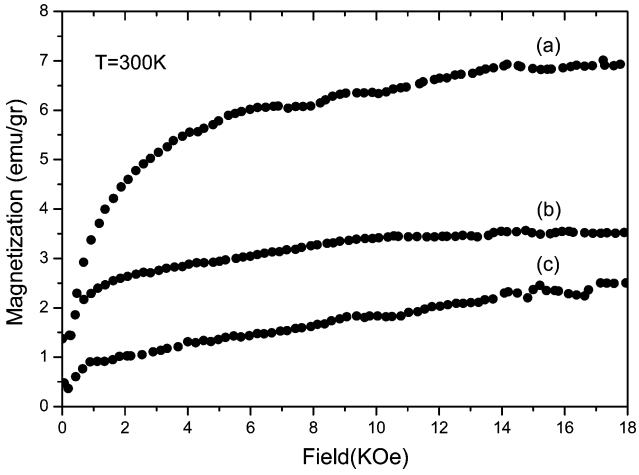

Fig. 4 Magnetization *versus* applied field curves for the samples: Almag-N17 (a), Almag-air17 (b) and Almag-O17 (c).

magnetic γ-Fe_2O_3 or produces magnetite (Fe_3O_4) nanocrystallites, if calcination takes place in an inert atmosphere. Therefore, complexation of the trivalent iron centers by the carboxylate moieties[42] is essential prior to transformation to each particular magnetic phase after pyrolysis. According to other reports, the key step for this kind of transformation is the reduction of the parent trivalent iron centers to their divalent state by the carboxylate units, the reducing power of which is well known in the literature.[43] More specifically, magnetite is first formed through ion re-organization and re-crystallization and subsequently γ-Fe_2O_3 is formed *via* oxidation of magnetite, provided that oxygen is present throughout the reaction process.[44] In our work, the pyrolysis of the alumina/iron–acetate system takes place under three different atmospheres, *i.e.* (a) an inert atmosphere, (b) air (significant amount of oxygen) and (c) 100% oxygen, and thus it is expected that magnetite, γ-Fe_2O_3 or α-Fe_2O_3 based alumina composites could be synthesized. Thus, the observed differences in saturation magnetization for the three composites of Fig. 4 can be attributed to the specific magnetic phases which have developed in each composite.

The questions that emerge at this point concern the size and the state of dispersion of magnetic particles into the pores of alumina. Magnetic measurements provide evidence for the size and interactions of the magnetic nanoparticles. According to theory, if a random assembly of small particles is cooled down under an applied field, the magnetic moment vectors tend to freeze parallel to the field. Upon increasing the temperature, the magnetization will decrease due to relaxation (M_{FC} curve). If the same process takes place without the application of a magnetic field, the magnetic moments are distributed randomly. If a small static field is applied, the magnetic moments tend to align along the field, so magnetization will also increase, but as the temperature increases the effect of relaxation will result in the decrease of the total magnetization (M_{ZFC} curve). The temperature (T_{max}) corresponding to the maximum in the M_{ZFC} curve is the blocking temperature and is related to a certain averaged volume of magnetic particles. Such behavior is characteristic of superparamagnetism and it is due to the progressive blocking of the magnetization of smaller and smaller particles as the temperature decreases. Along these lines, the zero field cooled magnetization M_{ZFC} and field cooled magnetization M_{FC} of the Almag-N17 sample are shown in Fig. 5. As shown in this figure, superparamagnetic behavior is observed, *i.e.* at high temperature the two curves coincide, while at lower temperatures $T_{bra} \sim 120$ K (T_{bra} is the branching temperature) M_{ZFC} and M_{FC} start to separate, where the M_{ZFC} magnetization shows a broad maximum. In addition, the M_{FC} curve increases up to T_{max} and then saturates, while the ratio T_{bra}/T_{max} is almost 1. According to the above comments we can assign the observed curves to small magnetic particles exhibiting maximum interactions and therefore strong aggregation.[45] Similar behavior was observed for the other two composites with the exception of a different T_{bra}.

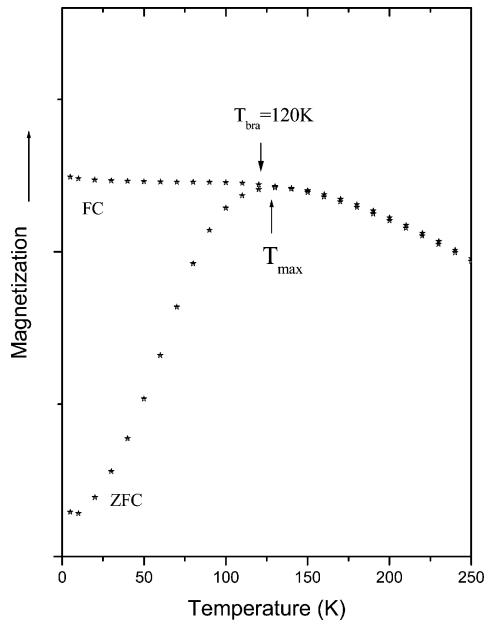

Fig. 5 Thermal variation of zero field cooled (ZFC) and field cooled (FC) magnetization of magnetic particles in Almag-N17.

We used transmission electron microscopy (TEM) to investigate the nature of the magnetic nanoparticles in the composite materials. Shown in Fig. 6 are representative TEM images of the composites as well as that for the host porous alumina (Fig. 6a) for comparison. The TEM images of the composites Almag-air17 and Almag-N17 show that the magnetic γ-Fe_2O_3 nanoparticles are finely divided within the resulting material, Fig. 6b, c. It was not possible to distinguish between the iron and alumina oxidic structures in the nanometer scale length. The results clearly indicate that the magnetic nanoparticles in these materials are very small, in the range of a few nanometers. In contrast, for the sample calcined in oxygen (Almag-O17), the TEM reveals the formation of significant larger magnetic nanoparticles ($\sim$50 nm) clearly distinct from those of alumina, see Fig. 6d.

The nature and size evolution of the magnetic particles in Almag samples were studied by variable-temperature Mössbauer spectroscopy. Fig. 7 shows representative spectra of the Almag-air17 sample, recorded in the temperature range 4.2 to 300 K. The spectra show a gradual evolution from a paramagnetic doublet to a six-line spectrum as the temperature decreases. This behavior is typical of samples containing superparamagnetic particles.[46] According to theoretical models, superparamagnetic behavior occurs if the thermal energy k_BT is comparable with the anisotropy energy of the particles. The magnetization vector can fluctuate between the easy directions of magnetization of the particle, with a relaxation time that follows an Arrhenius equation:

$$\tau = \tau_o \exp KV/k_BT$$

where k_B is Boltzmann's constant, T the absolute temperature,

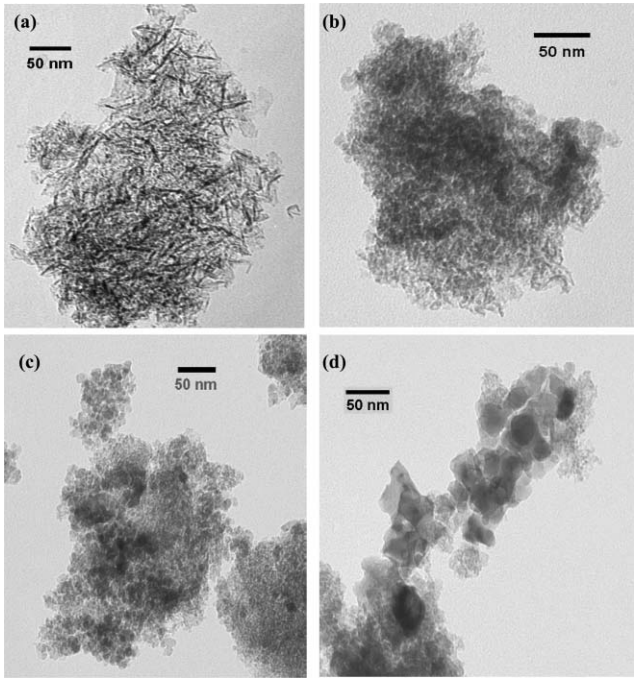

Fig. 6 TEM images of: (a) pure porous alumina, and magnetic alumina nanocomposites: (b) Almag-air17, (c) Almag-N17 and (d) Almag-O17.

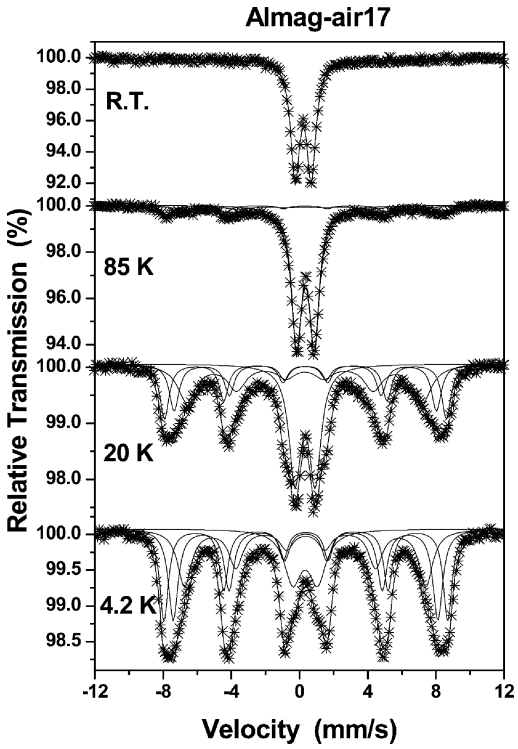

Fig. 7 Mössbauer spectra of Almag-air17 sample recorded at room temperature, 85 K, 20 K and 4.2 K.

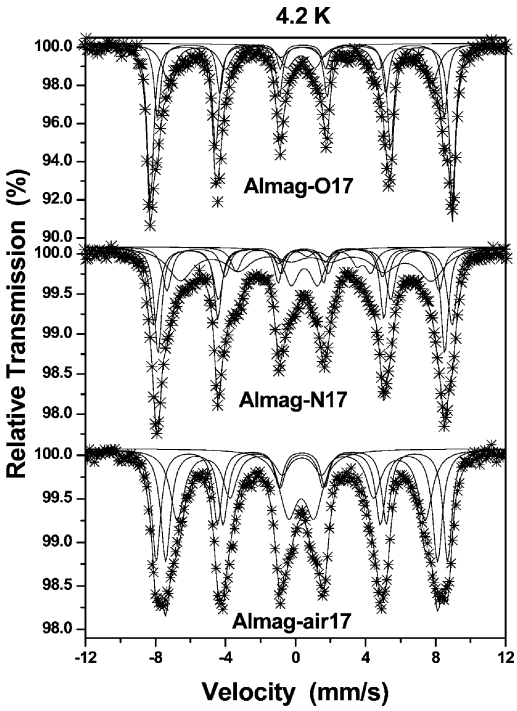

Fig. 8 Mössbauer spectra of Almag-air17, Almag-N17 and Almag-O17 samples recorded at 4.2 K.

K the effective anisotropy energy constant, V the volume of the particle and τ_o is a preexponential factor which is of the order of 10^{-9}–10^{-11} s. Superparamagnetic relaxation can conveniently be studied by using Mössbauer spectroscopy since it results in a broadening of the absorption lines for relaxation times of the order of 10^{-8} s, whereas for $\tau \leqslant 10^{-9}$ s the magnetic hyperfine splitting disappears. Thus, magnetic hyperfine fields can be measured by Mössbauer spectroscopy only if the time required for the measurements τ_{obs} corresponds to $\tau_L = {\omega_L}^{-1}$, where ω_L is the Larmor frequency of the nuclear spin. Therefore, for $\tau_L \ll \tau$, ferromagnetic behavior (sextet) and for $\tau \ll \tau_L$ superparamagnetism (singlet or doublet) will be observed. The temperature at which $\tau_L = \tau$ is the blocking temperature T_B and is often defined as the temperature at which 50% of the spectral area accounts for the magnetic part.

As shown in Fig. 7, the R.T. spectrum of Almag-air17 (T = 300 K) consists of one paramagnetic doublet only with isomer shift δ = 0.32 mm s^{-1} and quadrupole splitting ΔE_q = 0.95 mm s^{-1}, similar to that observed by Brown *et al.*[47] Both values suggest isolated paramagnetic Fe^{3+} centers in an octahedral oxygen coordination. At 85 K the spectrum of the same sample consists of a magnetic part in addition to the paramagnetic, with relative areas 28% and 72% respectively. At 20 K the magnetic part is more intense, with broad lines, in addition to the paramagnetic part. The simultaneous appearance of the paramagnetic doublet and the magnetic sextet in these spectra is characteristic of superparamagnetic behavior, which is typical for small particles. At 4.2 K the spectrum displays a paramagnetic doublet, accounting for 15% of the total area of the spectrum, while the magnetic part requires three magnetic sextets with approximately equal absorption areas for acceptable analysis. The area of the paramagnetic doublet decreases with decreasing temperature and this area is transferred to the magnetic components. According to the above description, the superparamagnetic patterns exhibited by the Almag-air17 composite reveal that the system consists of nanoscale magnetic particles with a distribution of sizes dispersed in the alumina matrix.

Fig. 8 presents the ^{57}Fe Mössbauer spectra of the Almag-O17, Almag-N17 and Almag-air17 samples at 4.2 K. All spectra consist of one paramagnetic doublet plus a magnetic part. The magnetic part requires three magnetic sextets with approximately equal absorption areas for acceptable analysis. The third hyperfine magnetic sextet which was necessary for the spectrum analysis could be attributed to another iron phase in the sample or the particle size distribution. The spectrum of the sample heated in an oxygen atmosphere has sharp absorption lines and the paramagnetic area accounts for 8%. For the sample heated in nitrogen the paramagnetic area is 10% and the spectral lines are broader. For the air-heated sample the absorption lines become even broader and the paramagnetic contribution accounts for 15% at this temperature. The paramagnetic area contribution at this temperature arises from very small particles that do not order magnetically, due to their small size. The observed difference in the paramagnetic area between the three samples is attributed to the preparation procedure and more specifically to the atmosphere during heating, since all samples originate from the same preparation batch. Therefore, we can conclude that heating in air produces smaller particles than heating in nitrogen or in oxygen gas flow, in agreement with the TEM images.

As far as the nature of the magnetic particles is concerned, it is observed that all spectra are fitted by at least one broad doublet and three or four sextets having different Mössbauer parameters. The values of magnetic field (H), isomer shift (δ), quadrupole splitting (ΔE_q) and relative area % for each component of the spectra measured at 4.2 K are given in Table 2. The Almag samples exhibited completely different spectra at 4.2 K. The hyperfine values of the magnetic components of Almag-O17 are very close to those of hematite (α-Fe_2O_3)[16,48] while the corresponding magnetic components of Almag-air17 have hyperfine values similar to those of maghemite (γ-Fe_2O_3).[16,49] Hematite exhibits larger quadrupole splitting ($\Delta E_q \sim -0.11$ mm s^{-1}) as opposed to almost zero quadrapole splitting of γ-Fe_2O_3. Finally, the Mössbauer spectrum of Almag-N17 was fitted by magnetic sextets having isomer shift values of almost 0.6 mm s^{-1} which is characteristic of magnetite (Fe_3O_4).[50] The SQUID measurements discussed above provide additional support for the existence of these phases as the main phases in the three

Table 2 Mössbauer parameters resulting from least squares fits of the 4.2 K spectra of Almag-air17, Almag-N17 and Almag-O17 samples

	H/T	δ_{Fe}/mm s^{-1}	ΔE_q/mm s^{-1}	Area (%)
Almag-air17	—	0.43	1.46	15
	51.7	0.47	0.00	27
	48.2	0.46	−0.01	30
	44.0	0.45	−0.03	28
Almag-N17	—	0.58	1.58	9
	52.6	0.58	−0.07	26
	50.8	0.43	0.02	24
	47.9	0.60	−0.09	15
	42.1	0.63	0.01	26
Almag-O17	—	0.42	1.62	8
	53.6	0.49	−0.10	47
	51.0	0.47	−0.12	22
	46.9	0.43	−0.08	23

samples. Almag-N17 containing magnetite as the main phase shows larger magnetization than Almag-air17 containing γ-Fe_2O_3 while the Almag-O17 with hematite as the main phase shows the poorest magnetization.

Finally, magnetic Fe_2O_3–Al_2O_3 composites with different iron loadings, higher and lower than 17% wt, were prepared and also examined. However the optimum value in magnetization and porosity was obtained in composites containing 17% wt iron.

Conclusions

Fe_2O_3–Al_2O_3 composites were prepared *via* interaction of acetic acid vapors with iron oxides dispersed on the surface of a sol–gel derived porous alumina. This preparation method leads to Fe_2O_3-containing aluminas, which combine high specific surface areas and a variety of iron oxide nanoparticles, depending on the atmospheric conditions during preparation. The experimental data from magnetic measurements and Mössbauer spectra showed that the major magnetic iron oxide phases in composites were γ-Fe_2O_3 and Fe_3O_4 after calcination in air and nitrogen atmospheres respectively. In contrast, α-Fe_2O_3 was obtained in an atmosphere rich in oxygen. Electron microscopy images indicated both the coexistence of particles with sizes from a few to 50 nm and a particle morphology that depends on the atmospheric conditions during thermal treatment.

Acknowledgements

The authors thank Dr A. Simopoulos (NCSR DEMOKRITOS) for the 4.2 K Mössbauer measurements and Dr I. Panagiotopoulos for the magnetic measurements.

References

1 L. M. Sheppard, in *Ceramic Transactions, Vol. 31, Porous Materials*, ed. K. Ishizaki, L. M. Sheppard, S. Okada, T. Hamasaki and B. Huybrechts, American Ceramic Society, Westerville, OH, 1993, p. 3.
2 I. Nettleship, *Key Eng. Mater.*, 1996, **122–124**, 305.
3 G. R. Doughty and D. Hind, *Key Eng. Mater.*, 1996, **122–124**, 145.
4 M. Schmidt and F. Schwertfeger, *J. Non-Cryst. Solids*, 1998, **225**, 364.
5 J. L. Dormann and D. Fiorani, *Magnetic Properties of Fine Particles*, Elsevier, North-Holland, Amsterdam, 1992, p. 213.
6 G. D. Stucky and J. MacDougall, *Science*, 1990, **247**, 669.
7 A. H. Morrish, *The Principles of Magnetism*, Wiley, New York, 1966, ch. 7.
8 L. Gunther, *Phys. World*, 1990, **3**, 28.
9 R. D. Shull, R. D. McMichael, L. J. Schwartzendruber and L. H. Bennett, in *Proceedings of the 7th International Cryocoolers Conference*, Philips Lab., Santa Fe, NM, 1992, p. 1133.
10 R. F. Ziolo, E. P. Giannelis, B. Weinstein, M. P. O'Horo, B. N. Ganguly, V. Mehrotra, M. W. Russel and D. R. Huffman, *Science*, 1992, **257**, 219.
11 R. D. Shull, *IEEE Trans. Magn.*, 1993, **29**, 2614.
12 P. J. Halling and P. Dunnill, *Enzyme Microb. Technol.*, 1980, **2**, 2.
13 R. Arshary, *Biomaterials*, 1993, **14**, 5.
14 P. J. Robinson, P. Dunnill and M. D. Lilly, *Biotechnol. Bioeng.*, 1973, **14**, 597.
15 I. P. Penchev and J. Y. Hristov, *Powder Technol.*, 1990, **61**, 103.
16 L. Zhang, G. Papaefthymiou and J. Y. Ying, *J. Phys. Chem. B*, 2001, **105**, 7414.
17 Y. Kurokawa, *Desalination*, 1982, **41**, 115.
18 Y. Kobayashi, D. Kawashima and A. Tomita, *Chem. Mater.*, 1997, **9**, 1887.
19 B. G. Potter Jr. and J. H. Simmons, *Phys. Rev. B*, 1988, **37**, 10838.
20 K. Tsunetomo, H. Nasu, H. Kitayama, A. Kawabuchi, Y. Osaka and K. Takiyama, *Jpn. J. Appl. Phys.*, 1989, **28**, 1928.
21 M. Kishida, K. Umakoshi, J. Ishiyama, H. Nagata and K. Wakabayashi, *Catal. Today*, 1966, **29**, 355.
22 A. P. Skoutelas, M. A. Karakassides and D. Petridis, *Chem. Mater.*, 1999, **11**, 2754.
23 A. Bourlinos, A. Simopoulos, D. Petridis, H. Okumura and G. Hadjipanayis, *Adv. Mater.*, 2001, **13**, 289.
24 S. S. Jewur and J. C. Kuriacose, *Thermochim. Acta*, 1977, **19**, 195.
25 E. A. Pinheiro, P. P. A. Filho and F. Galembeck, *Langmuir*, 1987, **3**, 445.
26 M. A. Burns and D. J. Graves, *Chem. Eng. Commun.*, 1988, **67**, 315.
27 V. S. Thompson and R. M. Worden, *Chem. Eng. Sci.*, 1997, **52**, 279.
28 Z. Al-Hassan, V. Ivanova, E. Dobreva, I. Penchev, J. Hristov, R. Rachev and R. Petrov, *J. Ferment. Bioeng.*, 1991, **71**, 1.
29 V. Ivanova, J. Y. Hristov, E. Dobreva, Z. Al-Hassan and I. P. Penchev, *Appl. Biochem. Biotechnol.*, 1996, **59**, 187.
30 L. Ji, J. Lin, K. Ltan and C. Zeng, *Chem. Mater.*, 2000, **12**, 931.
31 M. C. Rangel and F. Galembeck, *J. Catal.*, 1994, **145**, 364.
32 Y. Kobayashi, D. Kawashima and A. Tomita, *Chem. Mater.*, 1997, **9**, 1887.
33 I. Pitsch, W. Gebner, A. Bruckner, H. Mehner, S. Moehmel, D-C. Ueker and M-M. Pohl, *J. Mater. Chem.*, 2001, **11**, 2498.
34 A. Vazquez, T. Lopez, R. Gomez, X. Bokhimi, A. Morales and O. Novaro, *J. Solid State Chem.*, 1997, **128**, 161.
35 M. Kumagai and G. L. Messing, *J. Am. Ceram. Soc.*, 1985, **68**, 500.
36 F. W. Dynys and J. W. Halloran, *J. Am. Ceram. Soc.*, 1982, **65**, 442.
37 C. Duval, *Inogranic Thermogravimetric Analysis*, Elsevier, Amsterdam, 1963, p. 330.
38 H. Blorck, *Z. Anal. Chem.*, 1912, **51**, 674.
39 T. Abe, Y. Tachibana, T. Uematsu and M. Iwamoto, *J. Chem. Soc., Chem. Commun.*, 1995, 1617.
40 M. Fröba, R. Köhn and G. Bouffaud, *Chem. Mater.*, 1999, **11**, 2858.
41 K. Starke, *J. Inorg. Nucl. Chem.*, 1960, **13**, 254.
42 M. Takano, *J. Phys. Soc. Jpn.*, 1972, **33**, 1312.
43 R. C. Mehrotra and R. Bohra, *Metal Carboxylates*, Academic, New York, 1983.
44 F. del Monte, M. P. Morales, D. Levy, A. Fernandez, M. Ocaña, A. Roing, E. Molins, K. O'Grady and C. J. Serna, *Langmuir*, 1997, **13**, 3627.
45 E. Tronc, P. Prene, J. P. Jolivet, F. d'Orazio, F. Lucari, D. Fiorani, M. Godinho, R. Cherkaoui, M. Nogues and J. L. Dormann, *Hyperfine Interact.*, 1995, **95**, 129.
46 J. M. Coey and D. Khalafalla, *Phys. Status Solidi A*, 1972, **11**, 229.
47 I. W. M. Brown, K. J. D. Mackenzie and C. M. Cardile, *J. Mater. Sci. Lett.*, 1987, **6**, 535.
48 N. N. Greenwood and T. C. Gibb, *Mössbauer Spectroscopy*, Chapman and Hall, London, 1971, p. 241.
49 E. Murad, in *Magnetic properties of fine particles*, ed. J. Dormann and D. Fiorani, Elsevier, North-Holland, Amsterdam, 1992, p. 339.
50 G. M. da Costa, E. De Grave and R. E. Vandenberghe, *Hyperfine Interact.*, 1998, **117**, 207.